Energy & Environmental Science

Artificial inflation of apparent photocatalytic activity induced by catalyst-mass-normalization and a method to fairly compare heterojunction systems

Journal:	*Energy & Environmental Science*
Manuscript ID	EE-ART-02-2019-000452.R1
Article Type:	Paper
Date Submitted by the Author:	30-Mar-2019
Complete List of Authors:	Kunz, Larissa; Stanford University, Chemical Engineering Diroll, Benjamin; University of Pennsylvania, Chemistry Wrasman, Cody; Stanford University, Chemical Engineering Riscoe, Andrew; Stanford University, Chemical Engineering Majumdar, Arun; Stanford University, Mechanical Engineering Cargnello, Matteo; Stanford University, Chemical Engineering

Title

Artificial inflation of apparent photocatalytic activity induced by catalyst-mass-normalization and a method to fairly compare heterojunction systems†

Authors

Larissa Y. Kunz,[a] Benjamin T. Diroll,[b] Cody J. Wrasman,[a] Andrew R. Riscoe,[a] Arun Majumdar,[c] Matteo Cargnello*[d]

Abstract

Despite the potential of using photocatalysts to sustainably produce fuels and chemicals, overall reaction rates remain prohibitively low, largely limited by recombination of photogenerated electrons and holes. Past research on suppressing this recombination by the addition of co-catalysts or by the formation of heterojunctions has led to claims that rates show enhancement compared to the single-component, junction-free counterparts. However, comparing these systems is rendered difficult by the common practice of reporting rates on a catalyst mass basis. Using a model system of TiO_2 and g-C_3N_4 with Pt, here we show that normalizing photocatalytic rates by mass fails to provide mechanistic insight and can also artificially inflate the apparent performance of heterojunction systems—in our case, overestimating the enhancement by 24 ± 7%. This effect is caused by the non-linearity of light absorption with respect to the concentration of each light-absorbing component, according to Beer's law. This factor needs to be taken into account to verify if improvements in absolute activity correspond to intrinsic activity. To this end, a method is presented for approximating a system quantum yield from measured reaction rates under simulated solar or otherwise polychromatic light. A sensitivity analysis provides guidelines for reducing the artificial enhancement introduced by mass-normalization for any heterojunction system.

Broader Context

Solar fuels and photochemistry have become increasingly popular as the need for sustainable processes becomes more urgent. Since current photocatalytic processes still suffer from prohibitively low efficiencies, most work in the literature focuses on developing new materials to enhance efficiency. Unfortunately, the use of non-standardized photochemical reactor systems and the wide-spread practice of reporting activities on a catalyst-mass-basis, which does not provide direct mechanistic insight, make it difficult to meaningfully compare published results. We demonstrate how photocatalytic activity can be highly non-linear, one consequence of which is that the apparent activity of heterojunction systems can be artificially inflated if reported on a mass-normalized basis. More rigorous studies avoid this issue by reporting quantum yields, i.e., activities normalized to absorbed photons, but quantum yields are difficult to measure and are only reported for monochromatic light. To this end, we present an alternative normalization to fairly compare systems under full-spectrum solar irradiation or otherwise polychromatic light.

[a] Department of Chemical Engineering and SUNCAT Center for Interface Science and Catalysis, Stanford University, Stanford, CA 94305, USA
[b] Center of Nanoscale Materials, Argonne National Laboratory, Lemont, IL 60439, USA
[c] Department of Mechanical Engineering and Precourt Institute for Energy, Stanford University, Stanford, CA 94305, USA
[d] Department of Chemical Engineering and SUNCAT Center for Interface Science and Catalysis, Stanford University, Stanford, CA 94305, USA. E-mail: mcargn@stanford.edu

† Electronic supplementary information (ESI) available.

Introduction

In light of the need for sustainable processes to produce fuels and chemicals, efforts in using renewable energy resources to power chemical transformations have increased in recent years.[1] An increasingly popular approach is the use of solar energy to generate hydrocarbons (by means of CO_2 reduction) and H_2. To produce solar fuels, solar energy must be collected and appropriately converted, CO_2 must be captured (in the case of CO_2 reduction), and the feedstocks must be catalytically converted—all steps which require significant technological improvements for solar fuels to become economically viable.[2] Various pathways exist, including using concentrated solar to run high-temperature thermal reactions, photovoltaics (PV) powering electrochemical cells (e.g., PV-electrolyzers), and natural or artificial photosynthesis.[3] While PV-electrolysis offers the highest solar-to-hydrogen efficiency to date[4] and benefits from extensive work on PV cells,[5,6] photocatalysis has the potential to lower H_2 costs further by means of improved scalability, if the required technical hurdles are overcome.[7] Since direct water splitting as of yet remains difficult photocatalytically,[8] much work in the literature focuses on photoreforming of waste streams,[9] even plastics,[10] which can be effective electron donors. Photocatalysis offers the benefit of both capturing solar energy and converting it into chemical energy within a single system.[11]

However, photocatalytic systems suffer from low overall photonic efficiencies (defined as reaction products formed per total rate of incoming photons). Some of the best results in photonic efficiency are about 10% for certain exergonic heterogeneous reactions photocatalyzed by titania (TiO_2), which has both a long history as a photoactive material[12] and shows the most promise as a photocatalyst.[13] The challenges still plaguing the field are believed to be the result of slow charge migration from a localized exciton to a co-catalyst junction or reaction center[14] and fast competing electron-hole recombination.[13] Slow charge transfer kinetics become increasingly problematic for reactions requiring multiple electrons (or analogously holes).[15]

To suppress electron-hole recombination, one widely explored possibility is to introduce co-catalysts to accelerate the redox reactions and prevent the accumulation of free electrons and holes that will otherwise recombine even more readily—a difficult approach, given characteristic times of charge separation and recombination (see Scheme 1). Synthesizing composites to spatially separate the electrons and holes across heterojunctions between semiconductors is another popular approach. Nanostructuring photocatalysts to both reduce charge migration distances and create separate, favorable facets to which electrons and holes can migrate has also received attention.[16-20] These approaches are frequently combined, for instance by making physical mixtures of nanostructured semiconductors,[21] electrospinning a polymeric semiconductor onto nanofibers of another semiconductor,[22] and growing a semiconductor directly onto nanostructured crystals of another.[23,24]

The dominant means of reporting catalyst activity in such studies is based on a product rate per total mass of catalyst.[25-31] However, it is widely recognized that catalyst-mass-normalization does not account for effective absorption area, the nonlinearity of light travelling through an absorptive medium, and reflective and scattering contributions.[32] The appropriate metric for absolute catalytic activity should depend on the rate-limiting step. Assuming that transport of mass and light are not limiting, the relevant portion of the photocatalytic process occurring on a heterogeneous photocatalyst surface, shown in Scheme 1, is composed of four steps: i) light (of energy $h\nu$) absorption, on the attosecond timescale;[33] ii) relaxation of hot $[e^-/h^+]$ pairs to the band edges by electron-phonon coupling within $\sim 1ps$;[34] iii) charge separation into electrons (e^-) and holes (h^+) within one catalyst or across a heterojunction, on the nanosecond to microsecond timescale, and competing with recombination, typically on the nanosecond timescale; and iv) subsequent redox chemistry, where each reaction is associated with its own rate, typically on the millisecond to second timescale (further reactions are not shown in Scheme 1).[16,35,36]

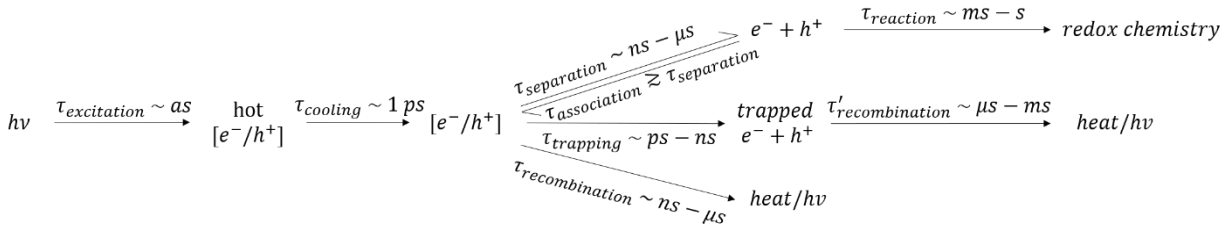

Scheme 1. Simplified schematic of the photocatalytic process.

Since surface redox chemistry is typically the slowest step,[37] the overall activity is sensitive to electron-hole separation and recombination kinetics governed by characteristic time constants $\tau_{separation}$, $\tau_{association}$, $\tau_{trapping}$, and $\tau_{recombination}$. As such, heterojunction systems are best compared by normalizing activity to the concentration of electron-hole pairs, $[e^-/h^+]$, or—as a more practical proxy—the rate of photons absorbed. Thus the rate of product formation per photon absorbed, known as the quantum yield (QY), provides information about a photocatalytic system intrinsic activity. Unfortunately QYs in heterogeneous photocatalytic systems are difficult to measure, and when they are reported, they are measured using monochromatic light.[25] However, the QY can vary with excitation wavelength, as evidenced by the dependence of photoluminescence QY on excitation energy,[38] and for photocatalytic systems being studied for direct use of incoming solar radiation, the QY matters across all wavelengths of the solar spectrum.

To address these issues, we present a normalization method that enables the approximation of QYs for polychromatic systems. We then apply it to a model system to demonstrate how normalization based on photocatalyst mass can artificially enhance performance. Titania (TiO_2) and graphitic carbon nitride (g-C_3N_4) (junction shown in Figure S1a) were chosen to comprise this model system due to extensive work in the literature on heterojunctions between them,[26] including a multitude of different morphologies.[21-24] Our normalization method is widely applicable to many different systems, thus making it appealing to improve research on photocatalytic systems for sustainable conversion of solar energy.

Experimental Methods

Materials

Dicyandiamide ($C_2H_4N_4$, 98.0%) was purchased from TCI. Oleylamine (OLAM, 98% and 70%), oleic acid (OLAC, 90%), and titanium(IV) chloride ($TiCl_4$, 99.0%) were purchased from Sigma-Aldrich. Octadecene (ODE, 90%) was ordered from Acros Organics, and N,N-dimethylformamide (DMF, 99.9%) was ordered from Fisher Scientific. Reagents were used as-received, and solvents were of reagent-grade.

Material Synthesis

Synthesis of carbon nitride. Graphitic carbon nitride (g-C_3N_4) was synthesized via thermal condensation of dicyandiamide following previously reported methods.[39] Between 100 mg and 500 mg of dicyandiamide were heated in a lidded 5 mL porcelain crucible to 550 ℃ at a ramp-rate of 8 ℃ min^{-1} in a nitrogen atmosphere and dwelling at 550 ℃ for 2 h, resulting in a hardened, yellow material.[39] The powder was then recovered, crushed, ground and sieved below 180 μm, and used for further characterization and testing.

Synthesis of TiO_2 nanocrystals. Scaling up a procedure previously reported,[40] brookite-phase TiO_2 nanorods were synthesized by a seed-mediated approach using standard Schlenk line techniques. 30 mL OLAM, 30 mL ODE, and 1.5 mL OLAC were first degassed (<2 torr) for 1 h at 120 ℃. After cooling the solution below 60 ℃ under nitrogen flow, 4.5 mL of a stock solution of 0.2 M $TiCl_4$ in degassed 1 M OLAC in ODE

(prepared in a glove box) were injected. The ensuing solution was heated to 290 ℃ and held 10 minutes to create the TiO_2 seeds, after which 12 mL of additional $TiCl_4$ stock solution were injected through a teflon tube at 0.3 mL min^{-1} to grow the rods, resulting in a shimmery, off-white to pale yellow solution. After cooling to below 100 ℃, the particles were twice washed with hexanes, precipitated with ethanol and centrifuged (8000 rpm, 3 min) before being redissolved in hexanes. The rods were then ligand-exchanged by addition of saturated $NOBF_4$ in acetonitrile under stirring (30 min) followed by centrifugation (8000 rpm, 5 min),[41] redissolved in DMF, and subsequently thermally treated identically to the g-C_3N_4 precursor.

Synthesis of the g-C_3N_4/TiO_2 composites. To make the composites, dicyandiamide and the ligand-exchanged titania nanoparticles were co-dissolved in DMF in various ratios, vacuum-dried overnight at 120 ℃, ground into a powder, and subsequently thermally treated identically to the g-C_3N_4 precursor. Note that high-TiO_2 composites are difficult to synthesize with the methods used in this study: based on accepted mechanisms for g-C_3N_4 formation,[42] a critical amount of dicyandiamide precursor seems to be needed between TiO_2 particulates to stabilize volatile melamine and melem intermediates and enable the formation of g-C_3N_4 (see Figure S1b).

All materials were ground and sieved with a 180 μm sieve after the thermal treatment. Replicate batches were synthesized of all samples to confirm reproducibility of material synthesis.

Material Characterization

Identity of the g-C_3N_4 was confirmed by transmission Fourier transform infrared (FTIR) spectroscopy, x-ray photoelectron spectroscopy (PHI VersaProbe 1 Scanning XPS Microprobe with a hemispherical electron analyzer, using Al(Kα) radiation and with spectra aligned to the adventitious C-C peak), and elemental analysis (Carlo Erba NA-1500 Elemental Analyzer).

Uniformity of the TiO_2 NP and the finalized catalysts was confirmed by transmission electron microscopy (TEM) using an FEI Tecnai G2 F20 X-TWIN with an Orius CCD camera. Scanning electron micrographs (SEM) were collected using the through-lens detector for secondary electrons of an FEI XL30 Sirion SEM. Absorbance spectra and band-gaps of the powdered and dispersed (in 0.2 M glycerol) catalysts were measured using an Agilent Cary 6000i UV/Vis/NIR. Fluorescence spectra of the g-C_3N_4 and composites dispersed in water were collected with a Horiba FluoroLog-3 Fluorimeter.

Final weight loadings of TiO_2 in the composites were determined by thermogravimetric analysis (TGA) in air in a TA Instrument Q500 by first holding the sample at 100 ℃ to remove any adsorbed water and then heating further to 650 ℃ to burn off the g-C_3N_4 until reaching a stable mass. Composites were further characterized for their BET surface area by first degassing the samples at 350 ℃ for 19 h in a Micromeritics Smart VacPrep and then performing physisorption in a Micromeritics 3Flex using N_2 as adsorbent at liquid nitrogen temperature. Grazing incidence X-ray diffraction of the composites was performed using a Bruker Single Crystal D8 Venture instrument.

Photocatalytic Activity under Simulated Solar Light

The catalysts were tested for glycerol photoreforming by dispersing them in a solution of 0.2 M glycerol in water in a quartz reactor with a stirring bar under a flowing inert Argon atmosphere using a solar simulating lamp (Newport 94021A Class ABB Solar Simulator with xenon lamp). High-concentration experiments were performed in 25 mL of reaction solution at about 0.85 mg-cat mL^{-1}, and low concentration experiments were performed at about 0.06 mg-cat mL^{-1}. Platinum nanoparticles were photodeposited onto the catalysts by adding 0.5wt. % (relative to the total catalyst mass) of Pt in the form of K_2PtCl_4 to each reaction mixture before any illumination of the sample was performed. Potential Pt residues were cleaned from the reactor and stirring bar between experiments by cleaning with aqua regia. Production of hydrogen was quantified with a Buck Scientific MultiGas #3 EPC gas chromatograph (GC) containing a HayeSep D column (using Ar as carrier) and a thermal conductivity detector and sampling every 6.6 min until reaching steady-state. Absorbance coefficients of the catalysts in 0.2 M glycerol were measured *in-situ* and under stirring, using

a Newport thermopile photodetector (3 W, model 919P-003-10) and parsing out absorption versus scattering from the bulk extinction coefficient by means of a 385 nm longpass filter and a neutral density NG1 filter (see Figures S2a-b); this method assumes that scattering does not depend strongly on wavelength within the solar spectrum, consistent with the predominance of Mie scattering with larger particle sizes. 95% confidence intervals in terms of hydrogen yield were calculated from time-on-stream at steady state for each experiment. A nominal value is used for the 95% confidence in TiO_2 mass fraction based on six replicate TGA measurements of a single composite sample; all other mass fractions were measured only once via TGA. All photocatalytic activity measurements reported at identical TiO_2 mass fractions in Figures 2 and 3 are replicate measurements of the same samples, performed to evaluate reproducibility of the results.

Photocatalytic Quantum Yield at 365 nm

Quantum yields at 365 nm in 0.2 M glycerol with 0.5 wt.% photodeposited Pt (by addition of K_2PtCl_4 to the reaction mixture in the QY reactor) were measured directly in a bubbled (Argon, through a porosity E frit) cylindrical reactor in an integrating sphere, as per the diagram in Figure S3. The sphere multiplier was found with a one-point calibration to the UV lamp total luminosity. Given the small reaction volume in this reactor (5 mL), a high catalyst concentration of about 2.3 mg-cat mL^{-1} was used. A PenRay model 90-0019-01 lamp was used with an Analytik Jena 99-0065-003 PS-6 power supply with output frequency 38 kHz. Light intensity was measured with a Thorlabs FD11A Si photodiode connected to a 0.1ms-RC-constant noise filter, the signals collected with a T7 LabJack (readings every 0.5s) and calibrated to the aforementioned Newport thermophile photodetector. Absorbance coefficients of the catalysts in this reactor were measured *in operando* (bubbling Argon) using the photodiode photodetector (Figures S2c-d). 95% confidence intervals in terms of QY were calculated from time-on-stream at steady state for each experiment. Reproducibility of QY measurements was evaluated by means of duplicate measurements of hydrogen yield and light absorption in the QY reactor for selected samples.

Time Resolved Photoluminescence

Time-resolved photoluminescence experiments were performed using ~30 fs excitation laser pulses at 400 nm and 2 kHz frequency, generated by frequency-doubling the output of a Spectraphysics Ti:sapphire amplifier. Photocatalytic powders were dispersed in deionized water in 1 mm quartz cuvettes for measurements, with the excitation and collection on the same side of the samples (front face geometry), with a 435 nm long-pass filter to block collection of scattered laser light. Photoluminescence was collected in free space with a focusing lens and directed into a Hamamatsu streak camera to record time-resolved data. As configured, the streak camera temporal resolution is ~500 ps. All counts in the visible spectrum were integrated to produce time-resolved data.

Results and Discussion

Theoretical treatment of light absorption in a heterojunction system

To compare photocatalytic activities, an ideal analytical reactor would be designed to account for light transport, electron-hole transport, and reaction kinetics, all of which contribute to overall rates. While directly measuring or even controlling each of these contributions is impractical, they can be modelled by coupled radiative transport equations at each wavelength (equation 1), electron-hole transport equations (equation 2), and a microkinetic model of catalytic activity (equation 3).

$$\frac{dI_\lambda(z)}{dz} = -\epsilon_\lambda I_\lambda(z) \quad (1)$$

$$\frac{\partial N_{e^-+h^+}(z,t)}{\partial t} = f_1\left(\sum_\lambda I_\lambda(z), N_{e^-+h^+}\right) \quad (2)$$

$$\frac{\partial N_{product}(z,t)}{\partial t} = f_2(N^\gamma_{e^-+h^+}) \quad (3)$$

Here I_λ and ϵ_λ are the light intensity and extinction coefficient at wavelength λ, $N_{e^-+h^+}$ is the number of separated electrons and holes, $N_{product}$ is the number of desired reaction product, z is distance along the light path length (e.g., depth, for a reactor illuminated from the top – see scheme 2), t is time, γ is the reaction order (typically one), and the full functional forms of f_1 and f_2 are catalyst- and reaction-dependent. This system is non-linear in space and time but can be approximately linearized within certain regimes. The length-scale is only introduced by light absorption. Defining d_λ as the characteristic length scale of light absorption at each wavelength, λ, the system can be approximated as linear in space if the light path length, l, is sufficiently small, such that $\frac{l}{d_\lambda} \ll 1$. Multiple time-scales (outlined in Scheme 1) dictate the functional form of the subsequent 3 equations, but they can be linearized by only considering steady-state measurements. With approximately linear behavior at each wavelength, results can be meaningfully compared across different systems using the same wavelength distribution: performance will scale nearly linearly with catalyst concentration.

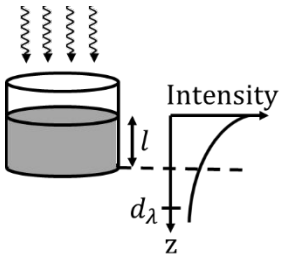

Scheme 2. Relevant length scales of light absorption, shown for a reactor illuminated from the top.

For experiments that are not conducted in this pseudo-linear regime (e.g., when there is need to increase absorption to improve signal-to-noise), the non-linearity in space can be removed by instead normalizing by the number of photons absorbed—i.e., the quantum yield. While polychromatic QYs are difficult to measure directly, we propose that they can be approximated by calculating the number of photons absorbed using the wavelength-dependent absorbance of the samples in solution. Let us consider a general case with an arbitrary number of photoabsorbers. The Beer-Lambert law can be extended to account for absorbance from all components at every wavelength:

$$N_{abs} = A\int n_\lambda\left(1 - e^{-\sum_i \sigma_{i,\lambda} c_i l}\right) d\lambda, \tag{4}$$

where N_{abs} is the number of absorbed photons, A is the irradiated area, n_λ is the number of photons between wavelengths λ and $\lambda + d\lambda$ in the incident light per unit area, l is the path length, and $\sigma_{i,\lambda}$ and c_i are the absorption cross section and number density (concentration) of photoabsorbing component i at wavelength λ, respectively. Inherent in the sum over all components is the assumption that the absorption of each component is not affected by the presence of other light-absorbing components. We now simplify this expression to just two photoabsorbers, but the rest of this analysis analogously applies to the extended case of any arbitrary number of photoabsorbers. Assuming that the absorption cross section σ_i has a negligible wavelength dependence at energies above the band gap (reasonable for the model g-C_3N_4/TiO_2 system, since the absorbance above the band gap can be considered approximately constant based on UV/Vis data shown in Figure S4), equation (4) simplifies to equation (5):

$$N_{abs} = N_{\lambda_1}\left(1 - e^{-\sigma_1 c_1 l - \sigma_2 c_2 l}\right) + (N_{\lambda_2} - N_{\lambda_1})(1 - e^{-\sigma_2 c_2 l}), \tag{5}$$

where N_{λ_i} is the total number of incident photons of energies greater than the band gap of photoabsorber i, E_i, corresponding to wavelength λ_i, with $E_1 > E_2$. The molecules of desired product produced can then be normalized to this number of photons absorbed.

While mass-normalized rates are naturally plotted versus mass-fractional catalyst composition, QYs are best plotted versus the component fractional photon-absorption. The fraction of photons absorbed by material 1, x_1, can be derived from the following set of equations (6a)-(6d), where L_1 and L_2 are the number of photons above energy E_1 absorbed by semiconductors 1 and 2, respectively, and M_2 is the number of photons between energies E_1 and E_2 absorbed by semiconductor 2; equations (6a)-(6d) describe the ratio of absorbed photons, the total number of absorbed photons above the larger band gap, the number of photons absorbed between the two band gaps, and the definition of x_1, respectively.

$$\frac{L_1}{L_2} = \frac{(1 - e^{-\sigma_1 c_1 l})}{(1 - e^{-\sigma_2 c_2 l})} \tag{6a}$$

$$L_1 + L_2 = N_{\lambda_1}(1 - e^{-\sigma_1 c_1 l - \sigma_2 c_2 l}) \tag{6b}$$

$$M_2 = (N_{\lambda_2} - N_{\lambda_1})(1 - e^{-\sigma_2 c_2 l}) \tag{6c}$$

$$x_1 = \frac{L_1}{L_1 + L_2 + M_2} \tag{6d}$$

Solving this system gives the following expression for x_1:

$$x_1 = \frac{N_{\lambda_1}(1 - e^{-\sigma_1 c_1 l - \sigma_2 c_2 l})(1 - e^{-\sigma_1 c_1 l})/(2 - e^{-\sigma_1 c_1 l} - e^{-\sigma_2 c_2 l})}{N_{\lambda_1}(1 - e^{-\sigma_1 c_1 l - \sigma_2 c_2 l}) + (N_{\lambda_2} - N_{\lambda_1})(1 - e^{-\sigma_2 c_2 l})}. \tag{7}$$

Using this framework, a linear correlation on a QY versus photon absorption fraction plot is representative of a "no-enhancement" system, in which the component photo-absorbers act independently of one another.

Applying the theoretical framework to the TiO_2/C_3N_4 case

This analysis can now be used to study the repercussions of operating outside the pseudo-linear regime. The repercussion we consider here is that choosing to mass-normalize activity in the spatially non-linear regime can artificially enhance the performance relative to the real, absorbed-photon-normalized performance. To demonstrate this effect, we consider a model system of composites of graphitic carbon nitride (g-C_3N_4) grown around TiO_2 nanoparticles.

The synthesis of carbon nitride yielded the sheet-like morphology shown with SEM in Figure 1a. The TiO_2 nanoparticles, as synthesized, demonstrate a morphology and uniformity by TEM characterization consistent with what is reported in the literature, though the morphology changes following the thermal treatment (Figure 1b).[40] The TiO_2 in the composites likewise loses its rod-like morphology after the thermal treatment (TEM, Figure 1c). While the TiO_2 and the g-C_3N_4 are in close contact in the composite, neither consistently wraps around or covers the other; as such, the effect of one component versus the other more directly facing the light source in the photocatalytic activity experiments should average out, assuming the dispersed particles are randomly oriented in the reaction solution. Photodeposited Pt nanoparticles seen in TEM of post-catalysis samples were consistently 1-2 nm in diameter, implying consistent co-catalyst morphology and hence activity.

The identity of g-C_3N_4 was confirmed by its IR absorption spectrum (Figure 1d), with tri-s-triazine breathing modes at 800 cm^{-1} and 890 cm^{-1}, various C-N/C=N stretching and breathing modes between 1205 cm^{-1} and 1630 cm^{-1}, and a broad feature around 3150 cm^{-1} attributable to N-H stretching. XPS also confirmed the synthesis of C_3N_4 with peaks (from high to low binding energy) in the C_{1s} spectrum (Figure 1e) attributed to a **π-π*** satellite, N-C=N groups, and C-C groups (from contamination, defects, or uncondensed precursor) and in the N_{1s} spectrum (Figure 1f) attributed to -NH_2, N-$(C)_3$, and C=N-C groups. The N_{1s} peak at ~404 eV has been attributed to a variety of causes in the literature, including C-NH groups,[43] local charge effects,[44-46] and -NH_2 groups.[47] The nitrogen-to-carbon ratio was determined by elemental analysis to be 4.5:3 and 4.6:3 for composites and bulk g-C_3N_4, respectively; this elevated ratio was likely caused by trapped byproduct ammonia and minimal residual precursor, as the nitrogen content is too high to be caused by terminal -NH and -NH_2 groups alone. This N:C ratio is comparable to what has been reported by others[48] and was found to be insensitive to thermal treatment dwell times between 1 and 4 h and temperature ramp rates between 5 °C min^{-1} and 20 °C min^{-1}. X-ray diffraction of the composites post-thermal treatment (Figure 1g) indicates the presence of brookite and anatase phases of TiO_2[49] as well as the

layering of carbon nitride sheets (peaks at 13° and 27.4°);[50] the reference XRD patterns in Figure 1g illustrate the beginning of the transformation of these TiO_2 nanorods from the brookite to the anatase phase upon heating in air at 600°C. BET surface areas of composites are lower than that of pure g-C_3N_4 but increase with increasing TiO_2 content at low overall TiO_2 weight loadings (Figure S5a). This observation suggests that the presence of TiO_2 renders the composite structure more compact, but increasing the amount of TiO_2 partly exfoliates the g-C_3N_4 layers of this more compact structure.

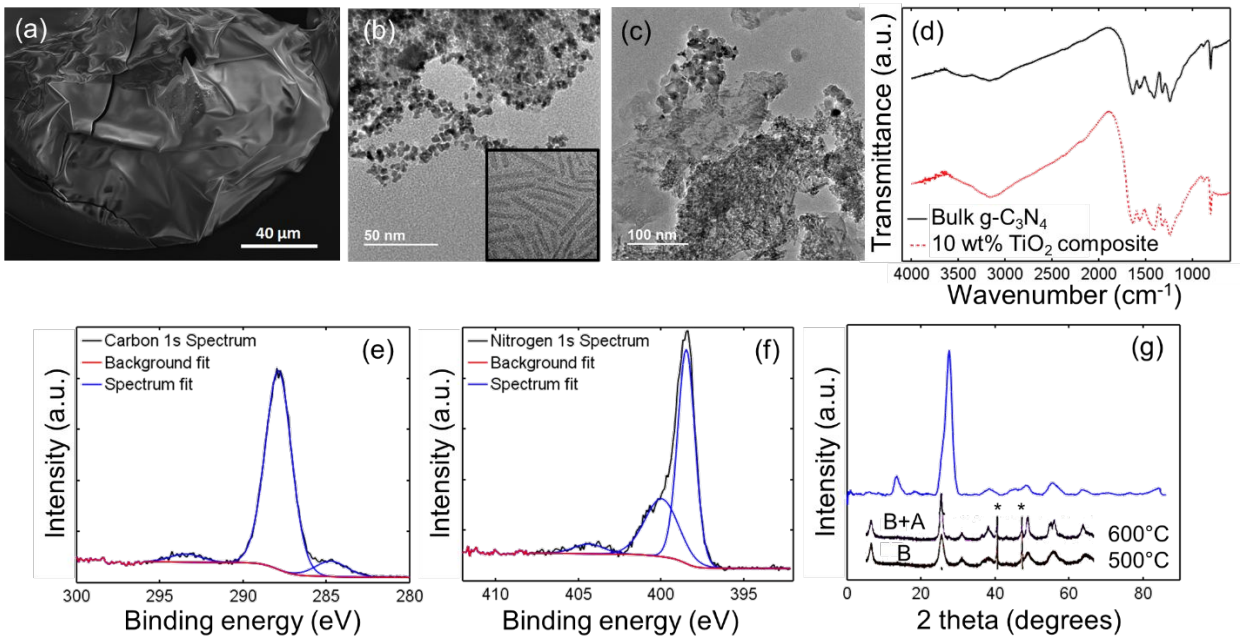

Figure 1. Characterization of the catalysts, including (a) SEM micrograph of layered g-C_3N_4 dropcast from a solution in concentrated sulfuric acid onto a silicon wafer; TEM micrographs of (b, inset) brookite TiO_2 nanorods, as synthesized, (b) thermally treated brookite TiO_2 (same scale bar as inset), and (c) a post-catalysis TiO_2 (30wt%)/g-C_3N_4 composite with photodeposited Pt; (d) FTIR spectrum of g-C_3N_4 and a TiO_2(10wt%)/g-C_3N_4 composite; (e) XPS C_{1s} spectrum and (f) N_{1s} spectrum of g-C_3N_4; (g) XRD of a TiO_2 (10wt%)/g-C_3N_4 composite, with reference spectra shown for TiO_2 nanorods heated (in the presence of Pt - the two starred peaks) in air, indicating brookite (B) and anatase (A) phases.

The UV-Vis absorption spectrum of powdered g-C_3N_4 indicates a 2.7 eV band gap (Figure S5b). The composite has a similar but smoother absorption profile, which could be caused by newly introduced defects, e.g., near junctions with TiO_2 or induced by changes in morphology and conjugation length.[51] The associated slight red-shift in the band gap does not significantly impact the fluorescence spectra (Figures S5c-f) of the composites relative to the bulk g-C_3N_4.

g-C_3N_4, TiO_2, composites of varying TiO_2 content, and physical mixtures of g-C_3N_4 and TiO_2 were tested for glycerol photoreforming, a means of converting aqueous glycerol solutions into H_2 and CO_2.[52] As shown in Figure 2a, catalyst-mass-normalized rates imply significant synergy, with multiple samples outperforming pure TiO_2. However, QYs directly measured at 365 nm suggest notably reduced synergy, with performance well below that of pure titania and at most 60% enhancement at low TiO_2 weight loadings (Figure 2b). Note that in calculating the absorption fraction, it is assumed that the absorption coefficients measured for the individual components, see Figure S2, likewise apply to the composites. The degree of synergy is quantified by means of a relative enhancement factor, φ, defined as the relative activity above a linear interpolation between endpoints (Figure 2b.ii). QYs measured at 365 nm and QYs approximated from the same experiments agree reasonably well, as shown in Figure S6c.

Duplicate measurements of samples at identical TiO_2 mass fractions (reported in Figure 2a) indicate a typical deviation less than 40 μmol/h/g-cat, significantly less than the observed apparent enhancement. For the direct QY measurements, duplicate measurements indicate typical variability in steady state hydrogen yields of 20 μmol/h/g-cat—corresponding to relative variability ranging from 25% for the less active g-C_3N_4 to as low as 2% for the more active, high-TiO_2 samples—and relative variability in light absorption below 3%. The resulting variability in the reported QYs is as high as ~25% for pure g-C_3N_4, decreasing to below 10% for the other, more active samples—approximately comparable to the 95% confidence intervals derived from time-on-stream at steady state reported in Figure 2b.

To enable a direct comparison between full-spectrum, mass-normalized activity and full-spectrum QYs, we apply the above analysis to approximate the polychromatic QYs, shown in Figure 2c. The linear interpolation between endpoints is the no-enhancement model and corresponds to the slightly curved no-enhancement plot in Figure 2a (calculated by reversing this normalization procedure for the model—multiplying QY by N_{abs} and then normalizing by an average mass characteristic of the high concentration experiments, and transforming the x-axis by numerically solving equation (7) for mass fraction, shown in Figure S6). Comparatively few samples now lie above the TiO_2 line. As shown in Figure 2d, normalizing by absorbed photons as opposed to catalyst mass consistently reduces the relative enhancement by 24 ± 7%. The remaining enhancement indicated by the approximated QYs, up to $\varphi = 1.45$ at a TiO_2 mass fraction of 30%, suggests real synergy between the co-catalysts. Variation between experiments at similar TiO_2 mass fractions is too large to precisely quantify the enhancement, but the QY-based synergy is comparable to the mass-normalized enhancement reported for some g-C_3N_4/TiO_2 systems and less than that reported for others.[26]

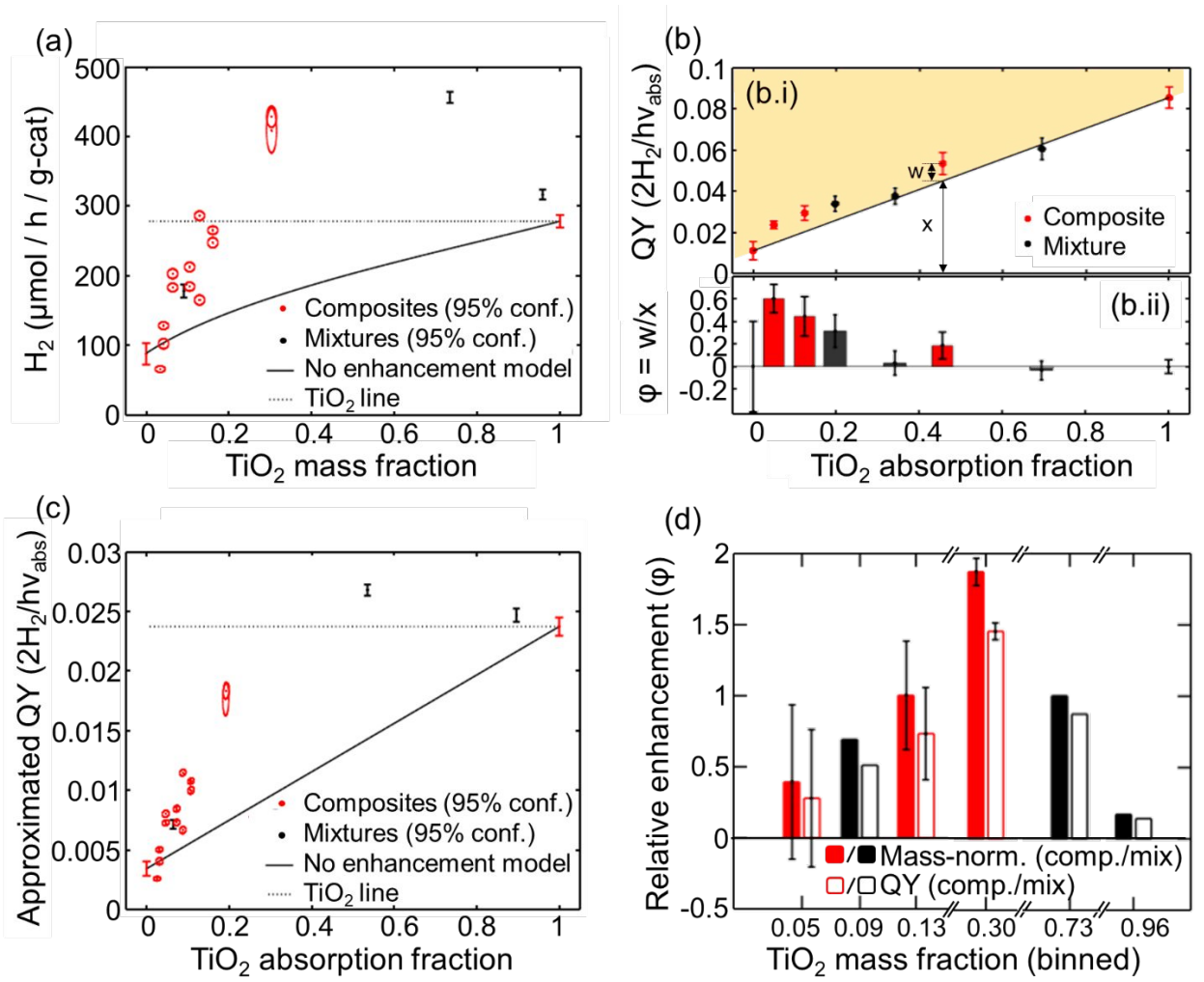

Figure 2. (a) Steady-state catalyst-mass-normalized photocatalytic activity of composites under simulated solar light compared to pure g-C_3N_4, pure TiO_2 (performance highlighted with a dashed reference line), and physical mixtures of the two. Error ellipses on composites represent 95% confidence intervals for each experiment, with error in H_2 calculated from variation with time on stream (at steady state) and a nominal value for error in TiO_2 mass fraction used based on six TGA measurements of a single composite; error bars for the physical mixtures and pure components are likewise 95% confidence intervals. (b.i) Directly measured QYs at 365 nm excitation wavelength of composites and mixtures with 95% confidence intervals; samples in the shaded region above the no-enhancement line (the line expected for two fully independent catalysts) demonstrate synergy whereas components of samples below that line impede the component performance. (b.ii.) The relative enhancement, φ, defined as $\varphi = w/x$, or the activity above the no-enhancement line, corresponding to each direct QY measurement. (c) Approximated QYs under simulated solar light, obtained by means of renormalizing the data in (a); error ellipses and error bars likewise portray 95% confidence intervals. The no-enhancement model indicates the QYs and mass-normalized rates that would be expected for g-C_3N_4 and TiO_2 acting entirely independently of one another. (d) Relative enhancement of composites and mixtures (from panels (a) and (c), divided into six bins) above a linear interpolation on a mass-normalized basis (solid bars) versus an absorbed-photon-basis (QY, open bars); here error bars correspond to one standard deviation of the collection of experiments within each bin.

The above full-spectrum experiments were performed in the spatially non-linear regime, at $\frac{l}{d}$~1 averaged over all wavelengths. The mass-normalization issue is expected to become negligible if we instead measure photoactivity in the linearizable regime. These experiments were thus repeated at a lower concentration,

such that $\frac{l}{d}$~0.1, as reported in Figure 3. The no enhancement model is approximately linear on the mass-normalized plot (Figure 3a), and the relative enhancement is only inflated by on average 3% in the mass-normalized case relative to the approximated QYs, as shown in Figure 3c. The low concentration polychromatic QYs are larger than those approximated from high concentration data, which can result from cross-shadowing effects and early-onset shadowing at selected wavelengths at high concentrations. The remaining, real synergy (Figure 3c) cannot be precisely quantified given the increased relative error of the low concentration measurements—hydrogen yields being nearly an order of magnitude lower than in the high concentration experiments, corresponding to relative error an order of magnitude higher—but suggests an enhancement ranging from 10% to 70%. Error bars reported in Figure 3c are calculated from the duplicate and triplicate measurements shown in Figures 3a and 3b.

Unlike the direct QY measurements and approximated low concentration QYs, high concentration data suggest a larger relative enhancement at higher TiO_2 mass fractions. This disparity might be caused by the onset of post-scattering absorption events with increasing TiO_2 content, analogous to secondary inner filter effects in fluorescence spectroscopy; this explanation is consistent with the earlier onset of shadowing effects with TiO_2 than g-C_3N_4 on a mass basis (see Figure S2).

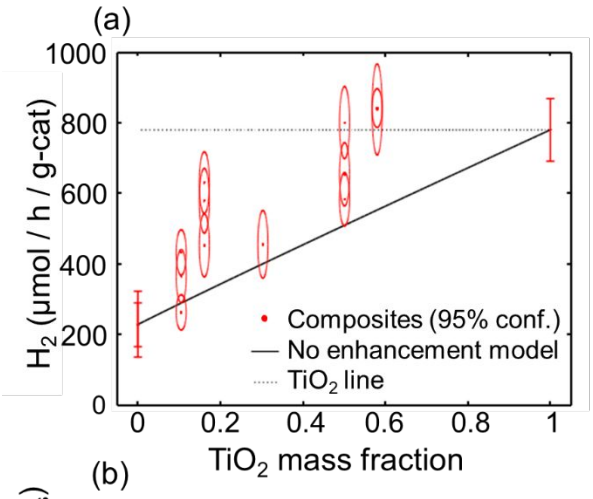

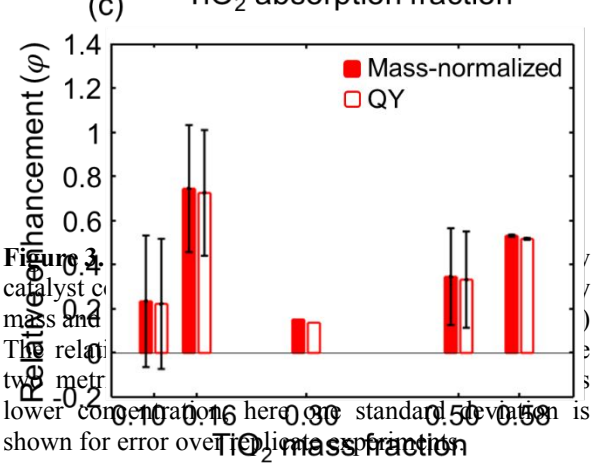

Figure 3. catalyst c… mass and … The relati… two metr… lower concentrations here, one standard deviation is shown for error over duplicate experiments.

To more directly probe the nature of synergy between the two semiconductors, the composites were characterized by transient photoluminescence, shown in Figure 4. For these measurements, the g-C_3N_4 was excited at 400 nm, where little or no TiO_2 absorption is expected. The photoluminescence dynamics of the pure g-C_3N_4 shows slower decay at early time compared to those of the composites, which likely indicates that at least some charge transfers, competing with intrinsic recombination mechanisms of g-C_3N_4. However, this competing transfer process is slow (τ_{CT} = 0.9-1.1 ns), and the quenched fraction of radiative recombination events is limited and varies between 30% and 60%. Note that due to significant scattering in these measurements, including variation between samples, quantitation of quenching is coarse. This result is consistent with the up to 70% increase in QY of hydrogen production above pure mixing models observed in the low concentration broadband illumination estimates, assuming quenching of photoluminescence g-C_3N_4 by charge transfer results in additional hydrogen production. Particularly

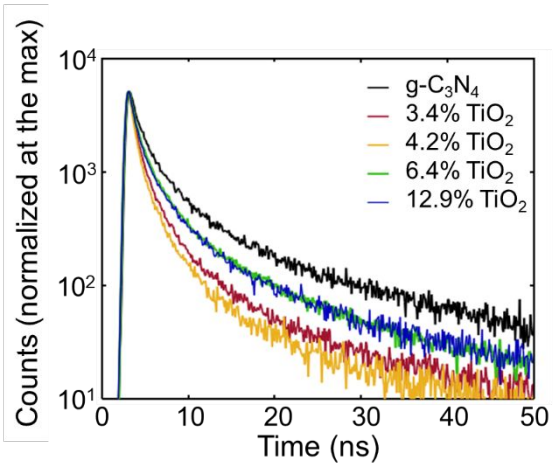

noteworthy is the non-linear fraction of quenching with sample composition, which is consistent with peak synergy at low TiO_2 fractions as measured at 365 nm excitation, but also underlining relatively ineffectual formation of charge-separating heterojunctions between the two materials. These data and the QY measurements strongly suggest that there is some small synergy between the two semiconductors but that the actual enhancement is notably reduced relative to the apparent, mass-normalized enhancement.

Figure 4. Transient photoluminescence of g-C_3N_4 and various composites with TiO_2 (composition reported by mass), normalized at the maximum photoluminescence.

Generalizing the model to arbitrary heterojunction systems

While the above g-C_3N_4/TiO_2 model system is misrepresented by normalizing the activity based on catalyst mass, the generality of this issue cannot be directly deduced. To that end, we generalize this analysis for an arbitrary heterojunction system. We consider a no-enhancement model, in which the QY of the composite system is described by a linear combination of the QYs of the two components, weighted by the photon absorption fraction. To transform this model to a mass-normalized basis, the QY normalization procedure outlined above was followed in reverse, numerically solving equation (7) for mass fractions from input photon absorption fractions and reversing the normalization in equation (5).

Matching the solar simulator reactor setup used in this study, this model assumes a light path length of 1 cm and an irradiation area of 16.6 cm^2 with light intensity of 1137 W m^{-2}, after filtering out the IR with an absorptive water layer. For the purposes of counting photons, the IR filter is approximated as a short-pass cut-off filter at 1013 nm. The photon and energy distributions used follow AM1.5 radiation, as shown in Figure S7. As it does not account for shadowing effects, this model is only valid for the regime in which $\frac{l}{d_\lambda} \lesssim 1$.

We analyze a generic two-photoabsorber system that is described by seven free variables: total catalyst concentration, $c = \sum c_i$, band gaps, E_1 and E_2, absorption cross-section, σ_1 and σ_2, and component QYs (for the reaction of interest), these latter three being key properties of the individual semiconductor photoabsorbers (SC1 and SC2). In the plots in Figure 5, each of these seven variables is separately treated as the free variable (or set of two free variables), while the others are fixed according to the values tabulated in Figure 5a. These values were chosen based on reasonable properties of the g-C_3N_4/TiO_2 system as well as other common systems in the literature, such as TiO_2/CdS. Specific absorption coefficients (as opposed to molar absorption coefficients) are used to match the practice of reporting catalyst concentrations by mass; as such, the absorption coefficient encompasses the catalyst molar mass.

Using this framework, we can define a relative artificial enhancement factor, ξ, as the fractional deviation of the no-enhancement curve from a linear interpolation between the individual components on a mass-normalized basis; ξ is analogous to the previously defined relative enhancement factor, φ, except that it only captures the artificial, mass-normalization-derived contribution. Symbolically, $\xi = u/x$, where x is the mass-normalized activity based on a linear interpolation, and u is the calculated mass-normalized activity above x (i.e., $u = \text{activity} - x$), as shown in Figure 5b. $Max(\xi)$ represents the maximum deviation from the linear interpolation along a mass fraction axis and hence the most severe artificial enhancement.

Consistent with the length scale argument, the no-enhancement model looks increasingly non-linear at higher concentrations (Figure 5b), as captured by the increasing $Max(\xi)$ plotted in Figure 5c. Similarly, the model sensitivity to the other model inputs - component band gaps, absorbances, and QYs - is captured in the plots in Figures 5d - 5f. Artificial enhancement is minimal when the two photoabsorbers have similar properties, as this situation approximates having only one photoabsorber, but becomes more pronounced as the properties of the two become increasingly different from one another.

The trends seen in Figure 5 can be explained intuitively. Catalyst particles at different depths receive different light intensity. A higher local concentration of photons implies a higher concentration of excitons

and thus larger absolute reaction rates and recombination rates. As one photoabsorber is exchanged for another, differences in their absorption properties change the light intensity profile through the reactor—change that is nonlinear with respect to mass fractional composition. Hence non-synergistic activity correlates nonlinearly with mass fractional composition.

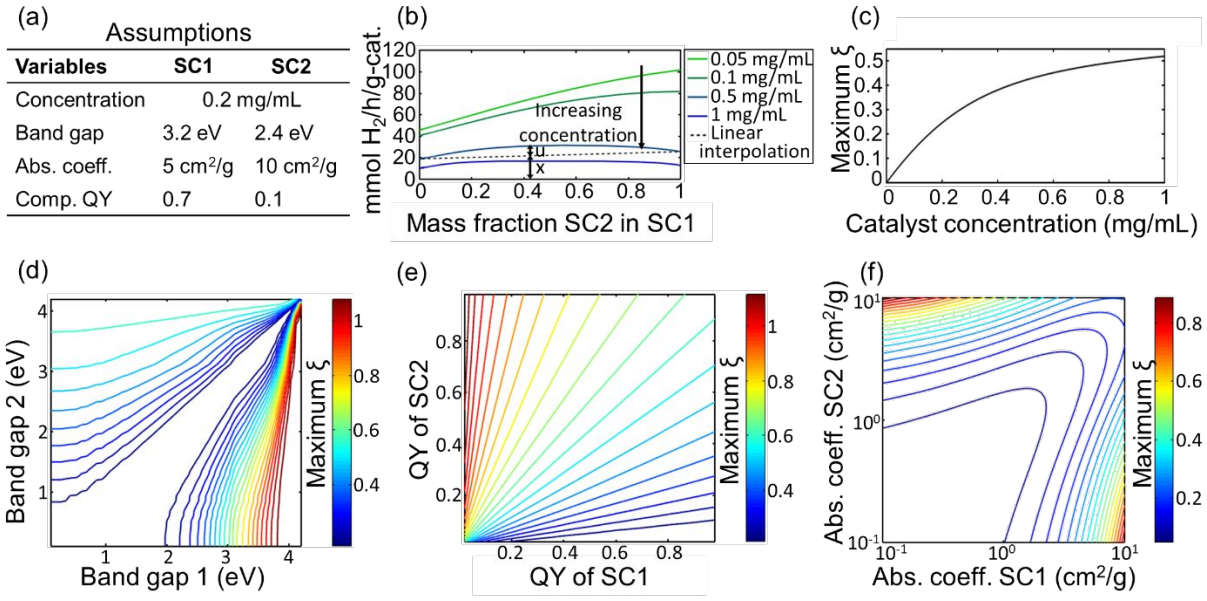

Figure 5. Artificial enhancement effect induced by normalizing photocatalytic activity by total catalyst mass of a two-photoabsorber system with no synergy. Key model parameters are tabulated in panel (a), with each variable being set as the free variable one-by-one in panels (c)-(f). Specific absorption coefficients are used to match the practice of reporting catalyst concentrations by mass. Sample mass-normalized curves are plotted in (b) for various total catalyst concentrations, and the relative enhancement factor, ξ (a function of mass fraction), is shown schematically for the 0.5 mg/mL case, defined as $\xi = u/x$. $Max(\xi)$ is plotted in panels (c)-(f). To avoid indeterminate solutions, band gaps, absorption coefficients, and quantum yields of zero are excluded.

The deviation from linearity tends to be positive because the total light absorbed scales with mass fractional composition as a convex function, $1 - e^{-c_{tot} l(\sigma_1 x_1 + \sigma_2(1-x_1))}$, where c_{tot} is the constant, total specific catalyst concentration, l is the light path length, and σ_i and x_i are the absorption coefficient and mass fraction of component i, respectively. Only in cases of equal absorption coefficients and band gaps (Figure 5e) will the light intensity profile remain constant as one component is exchanged for another; in this case the non-linearity is introduced by the transformation from mass-fraction to photon-absorption-fraction, following equation (7).

The results of the generic modeling in Figure 5 enable us to extract the following guidelines for avoiding this artificial enhancement.

1. Experiments should be performed in the linearizable $\frac{l}{d} \ll 1$ regime if operating at low concentrations and/or short path lengths for a given reactor setup is viable.
2. Mass normalization should not be used for sets of photoabsorbing materials whose absorption cross-sections differ by an order of magnitude or more. The magnitude of the artificial enhancement in such cases will of course depend on the band gaps and QYs of the components, as shown in Figure S8.

3. Mass normalization should be avoided in cases in which the smaller band gap material has a larger absorbance, as this magnifies the degree to which the light intensity profile through the reactor changes as one component is exchanged with another.
4. Both within and beyond the linearizable regime up until shadowing effects become significant, the analysis outlined above can be used to approximate the polychromatic QY instead of normalizing activity by catalyst mass.

Conclusions

While an ideal, analytical photocatalytic reactor would account for light transport, electron-hole transport, and reaction kinetics, measuring and controlling these individual contributions is difficult. A simpler approach is to model unavoidable non-linearities in the system and then use a mechanistically meaningful metric for reporting activity—namely, the quantum yield (QY) in the case of comparing heterojunction systems. To enable the use of this metric with polychromatic (especially solar simulating) systems, a method was developed for approximating polychromatic QYs.

This method, applied to a g-C_3N_4/TiO_2 model system, demonstrates one of the repercussions of operating outside the spatially linearizable regime: normalizing the activity of multi-photoabsorber systems by catalyst mass tends to artificially inflate the performance of these composite systems relative to their individual component counterparts. A general, no-enhancement heterojunction model was then generated, providing guidelines for reducing this artificial enhancement: experiments are best performed within the linearizable regime, $\frac{l}{d} \ll 1$, though the polychromatic QY can be approximated beyond this regime, as long as shadowing and multiple scattering effects are insignificant or quantifiable; mass-normalization should particularly be avoided when photoabsorbers have drastically different absorption cross-sections and when the smaller band gap material has the larger absorbance.

The proposed method for approximating QYs might enable the collection of more mechanistically meaningful photocatalytic data for heterojunction systems and identification of the true degree of synergism between co-catalysts.

Conflicts of Interest

There are no conflicts to declare.

Acknowledgments

L.Y.K. acknowledges support from a Stanford Graduate Fellowship (SGF), a TomKat seed grant from Stanford University, as well as NSF Eager Award #1732157. M.C. acknowledges support from the School of Engineering at Stanford University and from a Terman Faculty Fellowship. Part of this work was performed at the Stanford Nano Shared Facilities (SNSF), supported by the National Science Foundation under award ECCS-1542152. This work was performed, in part, at the Center for Nanoscale Materials, a U.S. Department of Energy Office of Science User Facility, and supported by the U.S. Department of Energy, Office of Science, under Contract No. DE-AC02-06CH11357.

References

[1] N. Lewis and D. Nocera, *PNAS*, 2006, **103**, 15729-15735.
[2] J. A. Herron, J. Kim, A. A. Upadhye, G. W. Huber, C. T. Maravelias, *Energy Environ. Sci.*, 2015, **8**, 126-157.
[3] R. J. Detz, J. N. H. Reek, B. C. C. van der Zwaan, *Energy Environ. Sci.*, 2018, **11**, 1653-1669.
[4] J. Jia, L. C. Seitz, J. D. Benck, Y. Huo, Y. Chen, J. W. D. Ng, T. Bilir, J. S. Harris, T. F. Jaramillo, *Nat. Commun.*, 2016, **7**, 13237.
[5] J. H. Montoya, L. C. Seitz, P. Chakthranont, A. Vojvodic, T. F. Jaramillo, J. K. Nørskov, *Nat. Mater.*, 2017, **16**, 70-81.
[6] A. Abate, J. Correa-Baena, M. Saliba, M. S. Su'ait, F. Bella, *Chem. Eur. J.*, 2018, **24**, 3083-3100.
[7] R. J. Detz, J. N. H. Reek, B. C. C. van der Zwaan, *Energy Environ. Sci.*, 2018, **11**, 1653-1669.
[8] F. A. Chowdhury, M. L. Trudeau, H. Guo, Z. Mi, *Nat. Commun.*, 2018, **9**, 1707.
[9] Z. Zhou, Z. Wu, Q. Xu, G. Zhao, *J. Mater. Chem. A*, 2017, **5**, 25450-25459.
[10] T. Uekert, M. F. Kuehnel, D. W. Wakerly, E. Reisner, *Energy Environ. Sci.*, 2018, **11**, 2853-2857.
[11] S. Kumar and L. Devi, *J. Phys. Chem. A*, 2011, **115**, 13211-13241.
[12] K. Hashimoto, H. Irie and A. Fujishima, *Jpn. J. Appl. Phys.*, 2005, **44**, 8269-8285.
[13] J. Schneider, M. Matsuoka, M. Takeuchi, J. Zhang, Y. Horiuchi, M. Anpo and D. Bahnemann, *Chem. Rev.*, 2014, **114**, 9919-9986.
[14] Y. Nakibli, Y. Mazal, Y. Dubi, M. Wächtler and L. Amirav, *Nano Lett.*, 2018, **18**, 357-364.
[15] H. Park, H. Kim, G. Moon, W. Choi, *Energy Environ. Sci.*, 2016, **9**, 411-433.
[16] Y. Tachibana, L. Vayssieres and J. R. Durrant, *Nature Photon.*, 2012, **6**, 511-518.
[17] M. Ni, M. K. H. Leung, D. Y. C. Leung and K. Sumathy, *Renew. Sust. Energy Rev.*, 2007, **11**, 401-425.
[18] H. Wang, L. Zhang, Z. Chen, J. Hu, S. Li, Z. Wang, J. Liu and X. Wang, *Chem. Soc. Rev.*, 2014, **43**, 5234 - 5244.
[19] M. Ge, J. Cai, J. Iocozzia, C. Cao, J. Huang, X. Zhang, J. Shen, S. Wang, S. Zhang, K. Zhang, Y. Lai and Z. Lin, *Int. J. Hydrogen Energy*, 2017, **42**, 8418-8449.
[20] S. Xie, Q. Zhang, G. Liu and Y. Wang, *Chem. Commun*, 2016, **52**, 35-59.
[21] B. Chai, T. Peng, J. Mao, K. Li and L. Zan, *Phys. Chem. Chem. Phys.*, 2012, **14**, 16745-16752.
[22] X. Wei, C. Shao, X. Li, N. Lu, K. Wang, Z. Zhang and Y. Liu, *Nanoscale*, 2016, **8**, 11034-11043.
[23] Z., Huang, Q. Sun, K. Lv, Z. Zhang, M. Li and B. Li, *Appl. Catal. B Environ.*, 2015, **164**, 420-427.
[24] L. Chen, X. Zhou, B. Jin, J. Luo, X. Xu, L. Zhang and Y. Hong, *Int. J. Hydr. Energy*, 2016, **41**, 7292-7300.
[25] J. Wen, J. Xie, X. Chen and X. Li, *Appl. Surf. Sci.*, 2017, **391**, 72-123.
[26] L. Zhou, L. Wang, J. Zhang, J. Lei and Y. Liu, *Res. Chem. Intermed.*, 2017, **43**, 2081-2101.
[27] D. Lu, H. Wang, X. Zhao, K. K. Kondamareddy, J. Ding, C. Li and P. Fang, *ACS Sustainable Chem. Eng.*, 2017, **5**, 1436-1445.
[28] H. Wei, W. A. McMaster, J. Z. Y. Tan, L. Cao, D. Chen and R. A. Caruso, *J. Phys. Chem. C.*, 2017, **121**, 22114-22122.
[29] N. Lu, C. Wang, B. Sun, Z. Gao and Y. Su, *Sep. and Purif. Tech.*, 2017, **186**, 226-232.
[30] Y. Di, X. Wang, A. Thomas and M. Antonietti, *ChemCatChem.*, 2010, **2**, 834-838.
[31] X. Wang, S. Blechert and M. Antonietti, *ACS Cat.*, 2012, **2**, 1596-1606.
[32] H. Kisch and D. Bahnemann, *J. Phys. Chem. Lett.*, 2015, **6**, 1907-1910.
[33] A. Föhlisch, P. Feulner, F. Hennies, A. Fink, D. Menzel, D. Sanchez-Portal, P. M. Echenique and W. Wurth, *Nature*, 2005, **436**, 373-376.
[34] W. Tisdale, K. J. Williams, B. A. Timp, D. J. Norris, E. S. Aydil and X.-Y. Zhu, *Science*, 2010, **328**, 1543-1547.

[35] X. Wang, Z. Feng, J. Shi, G. Jia, S. Shen, J. Zhou and C. Li, *Phys. Chem. Chem. Phys.*, 2010, **12**, 7083-7090.
[36] U. Gaya and A. Abdullah, *J. Photochem. and Photobio. C: Photochem. Rev.*, 2008, **9**, 1-12.
[37] J. Tang, J. R. Durrant and D. R. Klug, *JACS*, 2008, **130**, 13885-13891.
[38] J. Hoy, P. J. Morrison, L. K. Steinberg, W. E. Buhro and R. A. Loomis, *J. Phys. Chem. Lett.*, 2013, **4**, 2053-2060.
[39] J. Zou, L. Wang, J. Luo, Y. Nie, Q. Xing, X. Luo, H. Du, S. Luo and S. L. Suib, *Appl. Cat. B: Env.*, 2016, **193**, 103-109.
[40] M. Cargnello, T. Montini, S. Smolin, J. Priebe, J. J. D. Jaén, V. V. T. Doan-Nguyen, I. S. McKay, J. A. Schwalbe, M. Pohl, T. R. Gordon, Y. Lu, J. B. Baxter, A. Brückner, P. Fornasiero and C. B. Murray, *PNAS*, 2016, **113**, 3966-3971.
[41] A. Dong, X. Ye, J. Chen, Y. Kang, T. Gordon, J. M. Mikkawa and C. B. Murray, *JACS*, 2011, **133**, 998-1006.
[42] A. Thomas, A. Fischer, F. Goettmann, M. Antonietti, J. Müller, R. Schlögl and J. M. Carlsson, *J. Mater. Chem.*, 2008, **18**, 4893-4908.
[43] Z. Zhou, J. Wang, J. Yu, Y. Shen, Y. Li, A. Liu, S. Liu and Y. Zhang, *JACS*, 2015, **137**, 2179–2182.
[44] S., Yang, Y. Gong, J. Zhang, L. Zhan, L. Ma, Z. Fang, R. Vajtai, X. Wang and P. M. Ajayan, *Adv. Mater.*, 2013, **25**, 2452-2456.
[45] J. Liu, T. Zhang, Z. Wang, G. Dawson and W. Chen, *J. Mater. Chem.*, 2011, **21**, 14398-14401.
[46] M. Ye, Z. Zhao, Z. Hu, L. Liu, H. Ji, Z. Shen and T. Ma, *Angew. Chem. Int. Ed.*, 2017, **56**, 1-6.
[47] Y. Yuan, L. Zhang, J. Xing, M. I. B. Utama, X. Lu, K. Du, Y. Li, X. Hu, S. Wang, A. Genç, R. Dunin-Borkowski, J. Arbiol and Q. Xiong, *Nanoscale*, 2015, **7**, 12343-1250.
[48] X. Shi, M. Fujitsuka, Z. Lou, P. Zhang and T. Majima, *J. Mater. Chem. A.*, 2017, **5**, 9671-9681.
[49] R. Buonsanti, V. Grillo, E. Carlino, C. Giannini, T. Kipp, R. Cingolani and P. D. Cozzoli, *JACS*, 2008, **130**, 11223-11233.
[50] F. Fina, S. K. Callear, G. M. Carins and J. T. S. Irvine, *Chem. Mater.*, 2015, **27**, 2612-2618.
[51] M. Peer, M. Lusardi and K. F. Jensen, *Chem. Mater.*, 2017, **29**, 1496-1506.
[52] M. Cargnello, A. Gasparotto, V. Gombac, T. Montini, D. Barreca and P. Fornasiero, *Eur. J. Inorg. Chem.*, 2011, **28**, 4309-4323.